Available online at www.sciencedirect.com
ScienceDirect
C. R. Physique 9 (2008) 624–641
COMPTES RENDUS PHYSIQUE
http://france.elsevier.com/direct/COMREN/

Synchrotron x-rays and condensed matter/Rayonnement X synchrotron et matière condensée

Advances in synchrotron hard X-ray based imaging

José Baruchel *, Pierre Bleuet, Alberto Bravin, Paola Coan, Enju Lima, Anders Madsen, Wolfgang Ludwig, Petra Pernot, Jean Susini

European Synchrotron Radiation Facility, BP 220, 38043 Grenoble, France

Available online 31 October 2007

Abstract

Modern synchrotron radiation (SR) sources have dramatically fostered the use of SR-based X-ray imaging. The relevant information such as density, chemical composition, chemical states, structure, and crystallographic perfection is mapped in two, or, increasingly, in three dimensions. The development of nano-science requires pushing spatial resolution down towards the nanoscale.

The present article describes a selection of hard X-ray imaging and microanalysis techniques that emerged over the last few years, by taking advantage of the flux and coherence of the SR beams, as well as exploiting the advances in X-ray optics and detectors, and the increased possibilities of computers (memory, speed). Examples are given to illustrate the opportunities associated with the use of these techniques, and a number of recent references are provided. ***To cite this article: J. Baruchel et al., C. R. Physique 9 (2008).***

© 2007 Académie des sciences. Published by Elsevier Masson SAS. All rights reserved.

Résumé

Progrès récents en imagerie synchrotron aux rayons X durs. Les sources modernes de rayonnement synchrotron ont permis un développement considérable de l'utilisation des techniques d'imagerie. Des paramètres importants de l'échantillon tels sa densité, composition chimique, état chimique, structure et perfection cristallographique sont cartographiés à deux et, de plus en plus, à trois dimensions. Le développement des nano-sciences exige des efforts pour atteindre une résolution spatiale nanométrique.

Cet article décrit une sélection de techniques d'imagerie et microanalyse utilisant des rayons X durs, qui se sont développées au cours des dernières années, grâce à l'utilisation du haut flux et cohérence des faisceaux synchrotron, tout en exploitant les avancées en optique des rayons X et détecteurs, et les performances accrues des ordinateurs (mémoire, vitesse). Cet article fournit des exemples montrant les possibilités de ces techniques, et de nombreuses références récentes. ***Pour citer cet article : J. Baruchel et al., C. R. Physique 9 (2008).***

© 2007 Académie des sciences. Published by Elsevier Masson SAS. All rights reserved.

Keywords: Synchrotron radiation; X-ray imaging

Mots-clés : Rayonnement synchrotron ; Imagerie aux rayons X

1. Introduction

The availability of third generation Synchrotron Radiation (SR) beams has led to a dramatic increase of the use of SR-based X-ray imaging. A substantial fraction of synchrotron radiation-based research is being carried out today

* Corresponding author.
E-mail address: baruchel@esrf.fr (J. Baruchel).

1631-0705/$ – see front matter © 2007 Académie des sciences. Published by Elsevier Masson SAS. All rights reserved.
doi:10.1016/j.crhy.2007.08.003

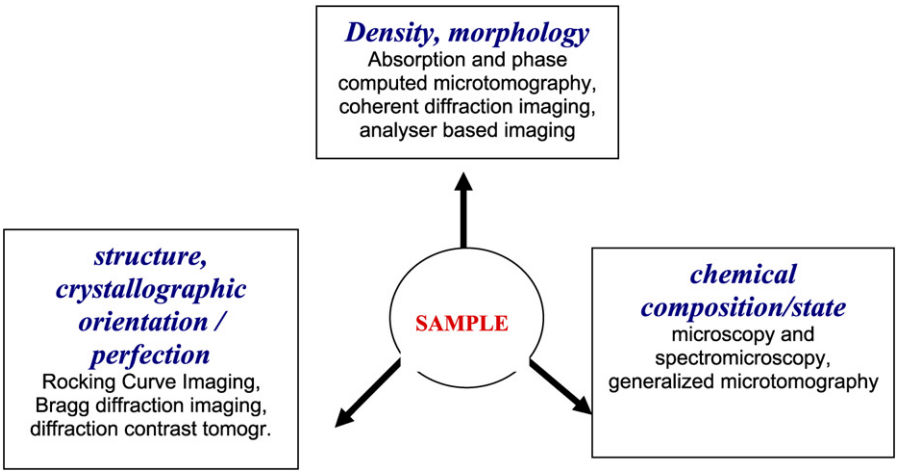

Fig. 1. Information accessible by using X-ray imaging, and some corresponding SR-based techniques.

with an 'imaging-type' approach, where the relevant information such as density, chemical composition, chemical states, structure, and crystallographic perfection (Fig. 1) is mapped in two, or, increasingly, in three dimensions. This approach corresponds to the fact that samples are not homogeneous, and that a 'local', in the μm or sub-μm range, characterization is needed. Many different scientific communities, such as materials science, soft condensed matter, biology, and cultural heritage, routinely employ, nowadays, these Hard Synchrotron X-rays Based Imaging techniques.

In addition, these X-ray imaging/microanalysis techniques follow an evident trend in the development of nanoscience by pushing spatial resolution down towards the nanoscale [1]. Hence, considering the concomitant developments of laboratory instruments and dedicated synchrotron beamlines worldwide (see for example [2,3]) a very competitive context can be anticipated for the coming years. Within this perspective, synchrotron based analytical techniques (diffraction, imaging and micro-spectroscopies) will play an important role by offering unique capabilities in the study of complex systems (local composition structure, perfection, and their evolution as a function of time or an external parameter).

The dramatic increase of the use of SR-based imaging/microanalysis techniques (see Table 1) is associated with the development of high spatial or temporal three-dimensional (3D) imaging, which is now accessible due to the simultaneous progress performed by X-ray sources, detectors, and computing facilities (memory, speed). A major factor in the development of SR-based X-ray imaging is the use of the coherence of the SR beams, which allows both a higher sensitivity and going towards higher spatial resolution. These techniques fully exploit the brilliance of the modern SR sources, and take advantage of the improvements of detectors and of new algorithms, in particular for the reconstruction of 'holotomographic' images, and for the iterative determination of the phase of the scattered amplitude

Table 1
Some of the emerging Sr-based X-ray imaging techniques, their requirements in terms of flux, coherence and nanofocussing, and the information they provide

	Flux	Coherence	Nanofocussing	Provided information
High resolution absorption microtomography	***			Density, morphology
Phase microtomography	***	***		Density, morphology
Coherent diffraction imaging	***	***	*	Density, morphology, structure, perfection
Analyser based imaging	***	**		Density, morphology
Microfluorescence	***		***	Chemical composition
Generalized tomography	***		***	Density, morphology, chemical composition
Spectromicroscopy	***		***	Chemical composition and state
Bragg diffraction imaging	***	**		Domains, phases, defects
Rocking curve imaging	***	*		Domains, phases, defects
Diffraction contrast tomography	***			Grain shape, orientation and perfection
X-ray projection microscopy	***	***	***	Density, morphology, structure, perfection

in 'coherent diffraction imaging'. Another approach utilizes, for phase contrast imaging, an analyser crystal ('analyser based imaging') that selects only a fraction of the beam refracted by a sample. This approach is clearly promising for medical and materials science applications.

The present generation of lenses used in the hard X-ray range (2–100 keV) has led to significant progress in the magnified and/or scanning version of X-ray imaging ('micro-nano-beam based imaging/analysis'). This is used for high spatial resolution 3D imaging ('X-ray projection microscopy'), and for chemically-selective X-ray imaging. A very interesting development is 'generalized tomography', which combines transmission, Compton, fluorescence and diffraction simultaneously.

The combination of imaging and Bragg diffraction, beyond the use of an analyser crystal, is another area where dramatic advances have been achieved. For single crystals, Bragg diffraction imaging, allows, when using coherent beams, one to access elusive information, such as the way domains match at the wall, or, when using the 'rocking curve imaging' approach, permits relevant physical parameters to be easily extracted locally. When dealing with polycrystalline materials the effort goes towards the implementation of a 3D technique capable of simultaneously providing data relevant to all of the length scales in the sample: local density and crystallographic structure, shape and orientation of the grains, and micro- or macroscopic strain and failure. A promising approach is diffraction contrast tomography, which allows the simultaneous investigation of damage, grain orientation and deformation.

The aim of the present article is to present most of the SR-based imaging techniques allowing access to (i) density and morphology; (ii) chemical composition and state; and (iii) structure and defects within the sample. In each case we will show the way these techniques rely on specific characteristics of modern SR beams, and emphasise the features not observable otherwise they can reveal. Recent references and, in most cases, a typical example, are given.

2. Density and morphology

When characterizing a sample a first, very important, information is its local morphology and density. This includes the shape of the various components (phases, inclusions, ...), as well as features like cracks or voids.

The behaviour of X-rays as they travel through an object can be described in terms of a complex index of refraction. In the X-ray region, it can be indicated as $n = 1 - \delta + i\beta$ where the real part δ corresponds to the phase shift (or refraction) and the imaginary part β to the absorption.

2.1. Absorption-based imaging

In most of the X-ray images ('radiography') the contrast results from variation in X-ray absorption arising from density differences and from variation in the thickness and composition of the specimen. The well-known Beer–Lambert exponential law describes this absorption process both for radiography and for expanding three-dimensional, tomographic, techniques.

The principle of microtomography is very similar to that of the medical scanner. It consists in recording a series of radiographs (typically of the order of 10^3) for different angular positions of the sample, which rotates around an axis perpendicular to the beam. Several laboratory microtomographs have been commercially produced over the last years, but the best images, in terms of spatial resolution, signal-to-noise ratio and quantitative exploitation, are obtained using the high intensity, practically parallel and monochromatic SR beams. In this approach there is no image magnification, and the spatial resolution mainly results from the effective pixel size of the detector (typically in the 0.3 μm to 30 μm range). Much effort is being produced to obtain the spatial resolutions in the 10–100 nm range. Several review papers that show how SR-based microtomography applies to different areas have been published recently (biomedical [4], materials [5], palaeontology [6]).

It is worth noting the substantial improvement in the temporal resolution of these microtomographic techniques associated to the use of SR beams. The time needed to record a complete microtomographic data set at a hard X-rays 3rd generation SR facility (ESRF in Europe, APS in the USA or Spring 8 in Japan), is not limited today by the SR X-ray flux. The already mentioned continuous development of X-ray detectors, and computing upgrades, lead to reductions in this time, which is now in the second range [7–9].

2.2. Phase contrast imaging, 'holotomography'

The real and imaginary parts of the index of refraction have very different dependence on the photon energy; in the regime where the photoelectric effect dominates and far from absorption edges, $\beta \sim E^{-4}$ while $\delta \sim E^{-2}$. As a consequence, the values of δ in the X-ray energy range are orders of magnitude larger than β terms. Exploiting δ in addition to β to produce images leads to a new type of imaging ('phase contrast images') that display an increased sensitivity. This usually requires a high degree of coherence of the X-ray beam. This results from the small source size σ (in the 50 μm range) and the large source to sample distance L (in the 100 m range). The transverse coherence length $d_c = \lambda L/2\sigma$, is in the 100 μm range, and allows 'phase images' to be recorded by just varying the sample-to-detector distance ('propagation technique', reviewed, for instance, in [15]). Fig. 2 shows, as an example, pores in a Al–Pd–Mn quasicrystal grain, on images recorded at several distances from the sample: only the biggest pores are visible on the first image, recorded at 13 mm, whereas smaller pores, with enhanced contrast, are observable on the images recorded when increasing the sample-to-detector distance.

This example shows that simple radiography allows us, when taking advantage of phase contrast, to investigate topics that were not accessible otherwise. Let us mention, in addition to the detailed study of pores in quasicrystals [10], and their evolution under thermal annealing [11] or melting and solidification [12] which give clues about the origin of the porosity, the investigation of high speed industrial sprays, which provide the experimental data to develop and validate liquid breakup models [13]. Grazing incidence reflectivity phase contrast imaging has also been demonstrated, the difference in optical path between terraces being in this case sufficient to observe monomolecular steps at a solid surface [14].

The easiest detectable features on phase contrast images are the 'edges' corresponding to phase jumps. They provide an important qualitative, or semi-quantitative, picture of the sample, but do not allow the extraction of quantitatively the local phase, and limit the spatial resolution through the occurrence of the fringes used to visualize the borders. A more quantitative approach of phase imaging and tomography is based on the combination of several images recorded at different distances. A phase retrieval algorithm allows, from these images, the 'holographic' reconstruction of the local phase [15]. Once the phase maps are obtained through holographic reconstruction, there is no conceptual difficulty in bringing together many maps corresponding to different orientations of the sample, and in producing the tomographic, three-dimensional, reconstruction procedure. The highest accessible spatial frequency is determined by the resolution of the detector. The capabilities of this parallel beam quantitative phase contrast imaging, called *holotomography* [16], were applied to a wide variety of materials, and constantly improved over the last few years. An example of what is achievable today is the first visualization of a 3D network for air circulation in seeds of the model plant *Arabidopsis* [17]. The value and number of the sample-to-detector distances, as well as the photon energy, were optimised [18]. New algorithms for mixed absorption/phase objects exhibiting both strongly and weakly absorbing areas (bone and soft tissue, for instance) are being implemented and lead to significant image enhancement [19].

The 'holotomography' approach can be combined with a magnification scheme to achieve sub-micron resolution. This rests on the use of a Kirkpatrick–Baez (KB) focussed pink beam and X-ray image magnification where the recorded images with different magnifications are numerically combined (phase retrieval) to obtain a magnified image

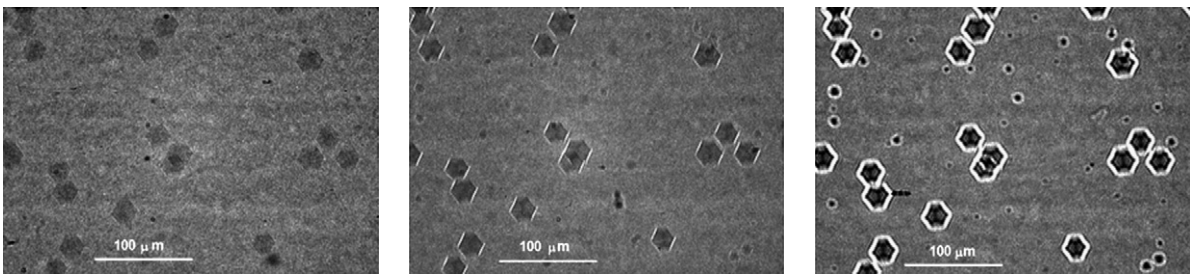

(a) (b) (c)

Fig. 2. Images of dodecahedral pores in a AlPdMn quasicrystal single grain, recorded at a sample-to-detector distance of (a) 13 mm, (b) 100 mm, (c) 500 mm.

displaying a pixel size of less than 100 nm. X-ray projection microscopy can be combined with tomography to obtain a 3D high spatial resolution image on a relevant region inside a laterally extended sample [20].

2.3. Coherent diffraction imaging (CDI)

The coherence properties of the X-rays may also be employed to beat the detector resolution in imaging by going into the far field (Fraunhofer diffraction) regime, as indicated on Fig. 3. In this case a strongly modulated intensity pattern, denoted a speckle pattern, is seen in the far field due to interference of the scattered radiation. The speckle pattern contains information about the spatial configuration within the scattering volume, while only averaged spatial information can be deduced from the incoherent scattering. One of the main applications of coherent diffraction is Coherent Diffraction Imaging (CDI).

CDI is a lensless imaging method with the aim of retrieving real space information from the speckle pattern. Since the scattered amplitude from the sample upon coherent illumination is the Fourier transform of the electron density, the image recovery is simply an inverse Fourier transform when the magnitude and the phase of the scattered amplitude are known. However, the phase is lost during the intensity measurement, and specific phase-retrieval algorithms must be used. Here, the resolution is not limited by an optical imaging system and diffraction-limited resolution is in principle possible. With the high penetration power of hard X-rays, the possibility of CDI to perform 3D imaging with nm resolution of e.g. biological samples and small crystals is unique. CDI with sub-50 nm resolution has been achieved in studies of e.g. freeze-dried cells [21], 3D composition of quantum dots [22], and strain inside nano-crystals [23]. An interesting possibility is to combine CDI with holographic approaches [24,25] to encode the phases and achieve a faster convergence of the algorithms.

Fig. 3 shows a typical experimental setup for CDI. A set of mirrors serve as high-energy X-ray filters, preventing higher-order monochromator reflections from reaching the sample and polluting the speckle pattern. All the optical elements are such that they do not to distort the wave front before the sample. An aperture, typically with an opening of 5 to 10 μm, i.e. smaller than the lateral coherence length d_c, is placed before the sample to select the coherent part of the monochromatized beam. After the aperture, a secondary aperture ('guard slit' in Fig. 3) is needed to block the stray scattering. The central cone emerging from the aperture illuminates the sample. A CCD camera measures the scattered intensity. A small beam-stop placed directly in front of the CCD prevents the direct beam from saturating the CCD pixels. The main experimental challenges are to reduce the unwanted scattering from the aperture and guard slit and to minimize the number of pixels shadowed by the beamstop.

Determining the phase of $E(Q)$ from measurements of $E(Q)E^*(Q)$ is a recurrent problem. In crystallography it is traditionally solved by replication of the structure in a periodic lattice. Iterative phase retrieval algorithms for isolated objects have been developed based upon earlier work [26,27]. The algorithms require an oversampled diffraction pattern, meaning that the speckle pattern must be sampled with a frequency at least twice smaller than $2\pi/R$ where R is the size of the scattering object (crystal, cell, etc.). This leaves a void area of zero-valued pixels outside the sample, but within the field of view of the CCD, which acts as constraint on the solution in real space. The constraint in Fourier space is the measured speckle pattern. By successive projections of these two constraints iteratively, the phasing algorithm can converge to a solution that satisfies both of them simultaneously. Several versions of the algorithm are in use and new approaches, such as the ptychographical iterative engine, are allowing the study of larger structures [28].

Fig. 4(a) shows the diffraction pattern of a test sample (ESRF logo) prepared by e-beam lithography and the reconstructed image is shown in Fig. 4(b). The half-period corresponding to the maximum scattering angle in the diffraction pattern is 34 nm and the oversampling ratio is about 5.5 in each dimension. The missing data in the central region (behind the beamstop) creates a difficulty for the convergence of the phasing algorithm, especially in the case

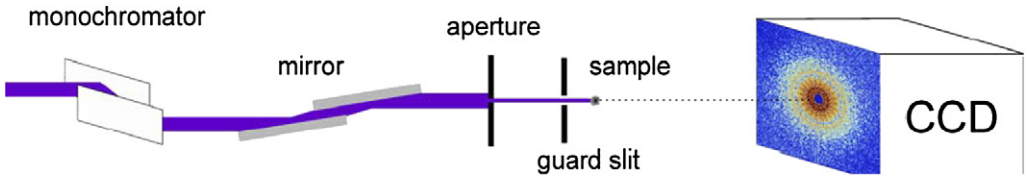

Fig. 3. Sketch of a typical setup for CDI with monochromator, mirrors and a beam defining aperture. The guard slit blocks the scattering from the aperture. The speckle pattern is usually measured by a 2D detector protected against the directly transmitted beam by a beamstop.

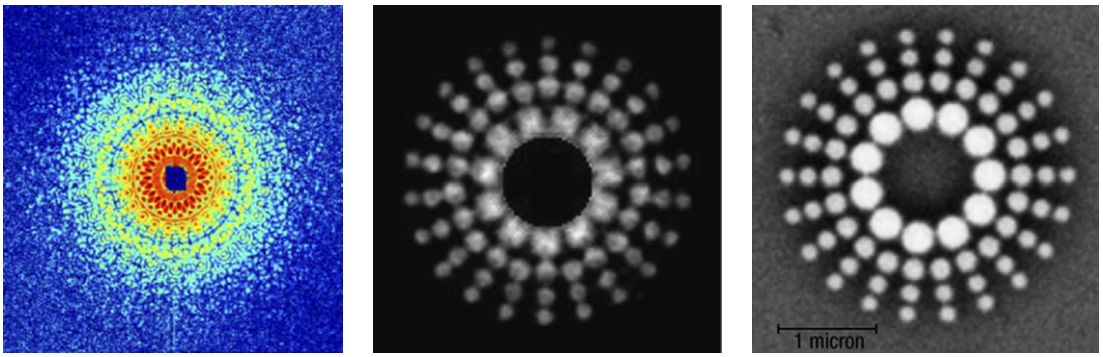

(a) (b) (c)

Fig. 4. (a) The measured diffraction pattern from a test sample with 7.3 keV X-rays at ID10A, ESRF and (b) the reconstructed image of the test sample (ESRF logo). (c) SEM image of the test sample.

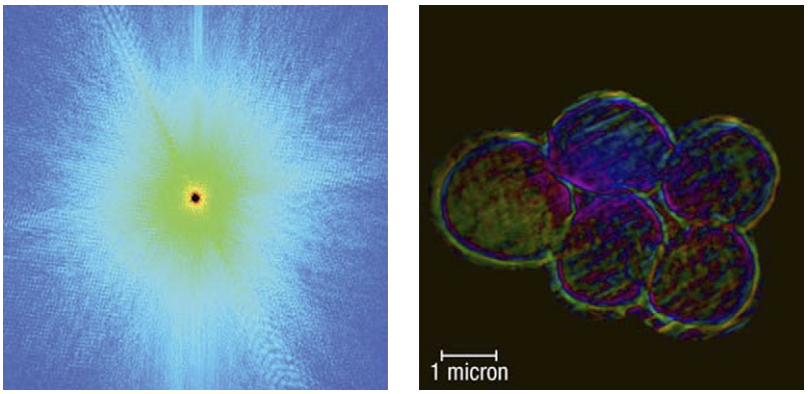

(a) (b)

Fig. 5. Coherent diffraction imaging of an assembly of yeast spores taken at ALS by the Stony Brook group [E. Lima, X. Huang, C. Jacobsen, J. Kirz, H. Miao, A.M. Nieman, A. Stewart, D. Sayre, D. Shapiro, 2006] with 520 eV X-rays: (a) measured diffraction pattern, (b) reconstructed image of 5 yeast spores. The brightness reflects the amplitude of the sample's exit wave and the hue represents its phase.

of symmetric samples, such as the logo shown here. The reconstruction in Fig. 4(b) was obtained after filling in the central missing data with the calculated Fourier magnitude taken from an SEM image of the sample, shown in Fig. 4(c) [29].

The potential of CDI in biological X-ray imaging has been demonstrated with dried samples [30,21]. Sample preparation in the frozen-hydrated state has the further advantage of preserving biological samples as close as possible to their natural state [31,32]. However, obtaining the necessary amorphous ice state (vitrification) in order not to disturb the cellular structure is difficult. Fig. 5 shows recent CDI results from the Stony Brook group, New York: (a) the measured diffraction pattern from frozen-hydrated yeast spores and (b) the reconstructed image, still in progress but clearly showing the membranes of the spores. However, the validity of the details of the reconstruction, such as the double membrane structure shown here, is unclear. The background signal from the ice matrix and the relatively low oversampling ratio of 3 to 4 in each dimension seem to be hindering the reconstruction in achieving a better resolution. Efforts to improve sample preparation techniques towards vitrification are ongoing and expected to improve the data quality. Furthermore, by going to hard X-ray CDI the Born approximation is fulfilled, and hence it is ensured that the reconstructed density corresponds to the true electron density of the sample.

2.4. Analyser based imaging

Analyser Based Imaging (ABI) is one of the phase contrast imaging techniques that has displayed a dramatic development over the last few years. Besides absorption, an X-ray beam traversing an object picks up information on its refraction properties that can also be utilized as a source of contrast for displaying the internal properties of

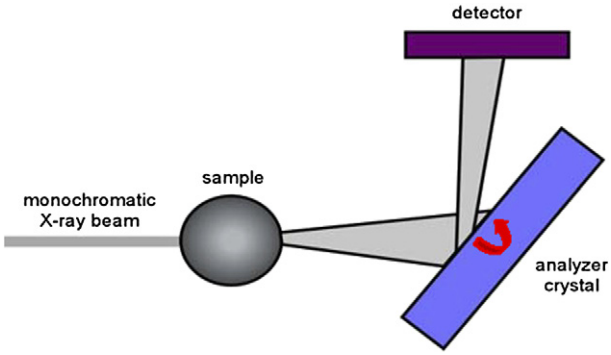

Fig. 6. Design of the experimental setup for analyser-based imaging: the sample-induced refraction of the beam is measured by rotating the analyser crystal and recording, for each angle and each of the pixels of the detector, the rocking curve.

the sample. Considering again the expression of the complex index of refraction $n = 1 - \delta + i\beta$, X-rays passing through regions of different δ values are subjected to phase shifts that correspond to being refracted. These changes can originate either from the shape of the object or from local homogeneity changes. They often cannot be visualized using absorption imaging techniques.

The analyser-based technique allows detecting these phase variations [33,34]. As shown on Fig. 6, the beam transmitted through a sample is analysed by a perfect crystal: on a given angle of the rotation of the analyser only the fraction of the beam satisfying the Bragg law for this analyser crystal can reach the detector and then contribute to the image formation. A complete data set corresponds to a rocking curve of the analyser for each of the pixels of the detector.

The angular resolution is provided by the choice of the analyser crystal and reflection. A typical order of magnitude is given by the full-width at half-maximum of the reflectivity curve for the reflection 111 of Si, at 60 keV, which worth 4 μrad.

The small angular acceptance of the analyser suppresses small-angle scattered radiation and thereby increases the signal to noise ratio. The edge enhancement, characteristic of this method, occurs at the interfaces of regions with different refractive index. It is achieved by slightly detuning the analyser away from the exact maximum of the reflectivity curve. In that way images can be recorded at angles which lie somewhat above and below the analyser maximum, for example at the half values of the maximum reflectivity where the reflectivity gradient is steepest. A ray that is refracted by a tiny amount when passing through a zone of changing refractive index is then reflected from the analyser with a considerably different reflectivity.

Quantitatively, to disentangle the information, Chapman and coworkers [35] proposed to form images of pure refraction $\Delta\theta$, and apparent absorption I_R, by linearly fitting the flanks the rocking curve (RC) obtained without sample, and solving the system $I_{L,H} = I_R R(\theta_{L,H} + \frac{\delta R}{\delta\theta}(\theta_{L,H}).\Delta\theta_z)$ where I_L and I_H are, respectively, the image intensities at $\theta_L = -1/2$ full width at half-maximum (FWHM) and $\theta_H = +1/2$ FWHM with respect to the centre of the RC. They called this approach 'Diffraction Enhanced Imaging'. However, this method omits considering the USAXS produced by the object.

To extract the angular deviation separately from absorption or USAXS, a *statistically based method*, was proposed [36]. It assumes that locally the angular distribution of the diffracted intensity is the convolution of the object angular spectrum with the analyser RC. Using N images taken along the RC, the method considers the individual RCs corresponding to each of the pixels of the detector (Fig. 7). In this case, two series of images are acquired, one with the sample and one without the sample, giving, respectively, for each individual pixel, an object RC and a reference RC. For each pixel, an algorithm calculates the zeroth-order moment M_0, equal to the integrated intensity, the first-order moment, which gives the centre of mass $\theta_0 = M_1/M_0$, and the second-order moment that yields the standard deviation $\sigma = (M_2/M_0 - \theta_0^2)^{1/2}$, as well as the maximum of the RC. Several experimental examples show that this pixel-by-pixel statistical method allows to independently extracting absorption, refraction, and scattering USAXS information.

The ABI technique has been widely applied in in vitro mammography and cartilage and bone studies. In *mammography*, fine details of the structures such as strands of collagen and contours between glandular and adipose tissue,

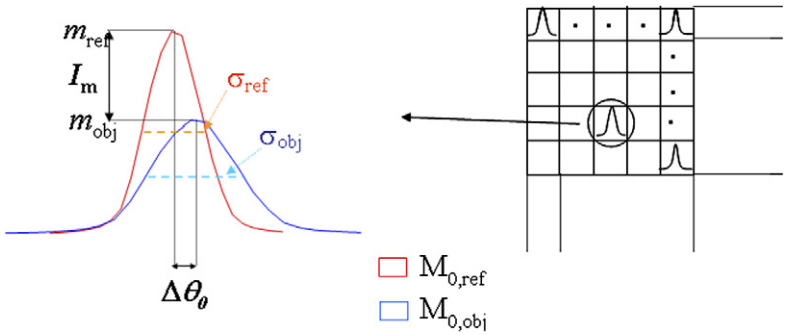

Fig. 7. In each pixel of the detector, the local RCs with object and without (reference) are recorded. The modifications in height (m_{ref} and m_{obj}), area, position $\Delta\theta_0$, and width (σ_{ref} and σ_{obj}) of this curve yield the information intrinsic to the object: the local absorption, refraction, and ultrasmall-angle scattering.

which are barely visible in the conventional absorption-based mammograms, are clearly visible in the analyser-based images. Images have been systematically compared with the stained histopathological sections; the correlation of the radiographic findings with the morphologic changes in specimens is unequivocally confirmed in several literature reports. Examples are found in [37–41]. An increased soft tissue contrast and a combination of information obtained with disparate diffraction-enhanced images provide better visibility of mammographically indistinguishable features. This kind of additional structural information of the breast tissue is required to improve assessment accuracy and earlier detection of the breast lesions. These advances in image quality make of ABI a promising candidate for clinical mammography at table-top sources.

ABI has been successfully applied for osteoarthritis *cartilage studies*. Osteoarthritis is a poorly understood disease that can affect the cartilage and other tissues in the joints of ageing people. Conventional radiography is sensitive only in cases of advanced disease in which there has been a loss of cartilage; structural abnormalities in the early stages of the degenerative process are generally not visualized in radiographs. Measurements have been performed on human articular cartilage in disarticulated, as well as in intact joints [42]. Cartilage defects, even at early stages of development, have been studied and compared with the absorption images: they show a clear, early visualization of the damage [43].

The ABI techniques have been recently extended through the use of two asymmetrically cut crystals mounted perpendicularly in the beam path, which achieve simultaneously analysis and magnification in both directions [44]. Guigay and co-workers proposed a theoretical treatment common to the ‘propagation’ and ‘analyser-based’ approaches [45].

2.5. *Detector-based analyser imaging*

An innovative phase contrast imaging technique, based on the use of an array-structured X-ray detector placed at a suitable distance from the sample, which simultaneously records and analyses the radiation refracted and scattered inside the object, is being developed.

Indeed the analyzer crystal used in the AB imaging can be considered as a slit system with an extremely narrow angular acceptance. On the basis of this observation, a further simplification can be conceived. In fact, a two-dimensional imaging detector, like a CCD camera, capable of independently reading and storing a given Region of Interest (ROI) of pixels, could be employed as a slits system. Each pixel line could act as a slit whose angular acceptance is given by the vertical Line Spread Function (LSF) of the detector.

In particular, if the X-ray beam incident on the sample has a vertical width equal to the vertical pixel size then the pixel line aligned with the incoming X-ray beam will detect the direct X-rays that have not interacted when passing through the sample (neither absorbed nor deflected) (e.g. line # 0 in Fig. 8); simultaneously the other pixel lines (e.g. lines # ±1 and ±2) above and below the central line will record the X-rays that have been deviated from their path (because of the refraction and scattering inside the object). The distance of a detector line from the central line corresponds to the angle of deviation, so that the angular distribution is recorded as by the analyzer crystal scan in ABI. When the sample is scanned through the incident fan beam the effects of refraction and scattering are mapped.

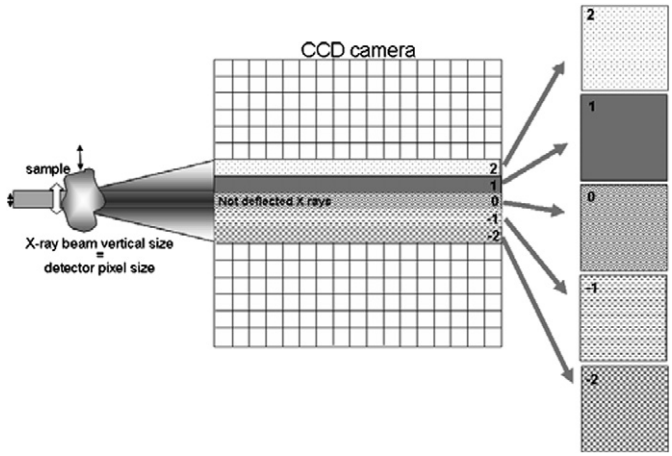

Fig. 8. Scheme of the detector-based analyzer imaging (DBA) modality. For more details, see text.

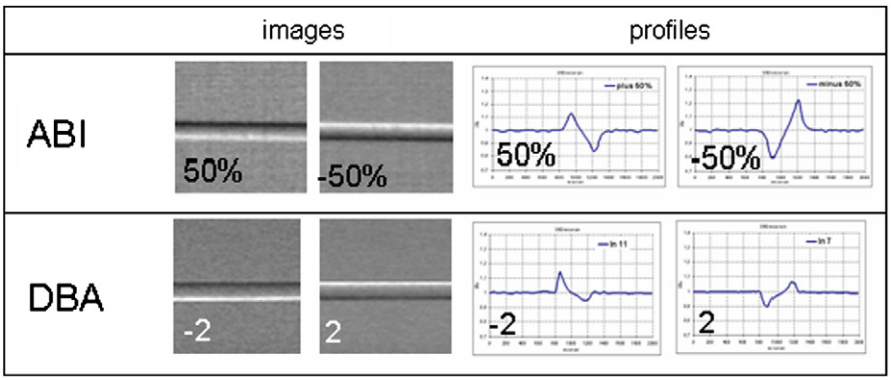

Fig. 9. Images and vertical signal profiles of a nylon fiber (350 μm diameter) acquired at 25 keV with the ABI (Si (111) analyzer crystal) and DBA (50 μm pixel size). For the ABI technique images corresponding to the ±50% positions are reported (positions indicated as percentage of the peak intensity of the crystal RC), while for the DBA technique the second line above and below the center line is shown corresponding to an angular acceptance of the range [8.6 μrad, 12.9 μrad].

Since this imaging modality is intrinsically linked to the detector properties, the technique is referred to as "detector-based analyzer imaging" (DBA) [46]. The preliminary tests and results on simple phase objects have highlighted that the detector-based analyzer imaging technique can produce images with features similar or equivalent to the analyzer-based imaging ones (see Fig. 9) with comparable signal-to-noise ratio values [46,47]. In addition, the DBA imaging, in its early implementation, also shows advantages with respect to the ABI: the stability of the optics is much more easily obtained and several refraction angles can simultaneously be acquired and analyzed. In fact, in a single acquired ROI, the refracted and scattered X-ray beam emerging from the irradiated portion of the sample is completely analyzed.

However, a few important optical requirements have to be fulfilled: the slit system and the array detector have to be perfectly aligned to avoid phase mixing, and a long sample-to-detector distance is needed in order to benefit from the wavefront free propagation and to have sufficient angular resolution. Moreover, particular care has to be taken to reduce the air scattering between the sample and the detector.

In order to fully understand the DBA signal, further theoretical and experimental investigations are required. The DBA may find applications in those fields where the requirements in terms of angular resolution are not so stringent but where a good optical stability is essential, as in the case of long exposure times and tomographic imaging.

3. Chemical composition and state

Over the past three decades, interest in X-ray microscopy revived, fostered by several major advances in X-ray sources and X-ray optics. In particular, X-ray imaging techniques largely benefit from the high brilliance of X-ray beams produced by third generation SR, which offer a control of the brightness, spectrum, geometry, polarization and coherence of the beam. Driven by these unprecedented properties of X-ray beams, concomitant progresses have been made in X-ray optics.

Hard and soft X-ray focusing optics are now reaching almost similar level of performance, with focused beam sizes below 50 nm [48–51]. However, these remarkable achievements remain at the demonstration stage and are still far from routine. Besides they have to be fully integrated into stable and reliable X-ray microscopes. Such implementations require not only outstanding quality optics, but also ultimate control of all experimental and environmental parameters (e.g. temperature, vibration, ...). It is worth noting that, in many cases, the probe dimensions (particularly in the horizontal direction) are no longer limited by the focusing device performance but rather by the geometrical laws of optics, i.e., the source size, the source-to-optics and optics-to-sample distances. For higher X-ray energies, this situation is aggravated when the optical devices display chromatic focusing behavior since the increase of the focal length with decreasing X-ray wavelength tends to lower the demagnification of the source image. The conception of long beamlines exceeding 100 m offers not only the possibility to produce small probes but also to obtain longer working distances, providing more space for specific sample environment. A major drawback of this scheme is the flux loss due to limited aperture of the focusing optics. The option of producing a secondary source (the synchrotron source is first demagnified into a secondary source which is itself demagnified again into a nano-probe) is a key-option in the management of the flux/beam size ratio. The current trends are the development of long beamlines and the use of either refractive lenses or multilayer coated mirrors in the Kirkpatrick–Baez geometry to access high energy [52].

As mentioned above, the development of high brilliance high-energy X-ray sources coupled with advances in manufacturing technologies of focusing optics has led to significant improvements in sub-micrometer probes for spectroscopy, diffraction and imaging applications in the multi-keV X-ray range. The main fields of application are driven by the unique attributes of X-ray microscopy in the multi-keV energy range: (i) access to K-absorption edges and fluorescence emission lines of medium-light elements and L-, M-edges of heavy materials for micro-spectroscopy, chemical or trace element mapping; (ii) higher penetration depths compared to soft X-rays or electrons allowing imaging of thicker samples or in-situ experiments; (iii) favorable wavelengths for diffraction studies; (iv) relatively long focal lengths and depths of focus which are advantageous for the use of specific sample environments (high pressure, controlled temperatures...). Compared to other techniques, synchrotron microprobes that measure the sample 'local' fluorescence and absorption (and also the diffraction or Compton scattering) display a unique combination of features [53]. In particular, the possibility of in-situ experiments remains a unique attribute of synchrotron based analytical methods. The photon penetration depth of hard X-rays enables specific sample environments to be developed to study realistic systems in their near-native environment rather than model systems. The ability to perform in-situ analysis with environmental chambers offering high or low temperature conditions, high pressure, or preserving sample hydration explains the increasing interest from communities such as Planetary and Earth sciences [54], environmental science. In this overall perspective, specific efforts have been made to integrate controlled sample environments into X-ray microprobe instruments: Cryo-cooling system for analysis of Antarctic ice [55], ultra low temperature cryostat (<10 K) for the study of semiconductors [56], micro-furnace for geochemistry at high temperature ($<700\,^{\circ}$C) [57]. Diamond Anvil Cells (DAC) are the most suitable apparatus for in-situ and real time studies at extreme conditions (0–10 GPa, 0–1000 °C) using X-ray fluorescence (XRF). Over the past five years, specific developments aimed at adapting the DAC to XRF geometry (detector at 90 degrees). This optimal angle of detection may either be obtained by using a partly drilled diamond [58] or by replacing one anvil by a diamond window and using an X-ray transparent gasket material [59]. Such improvements have allowed detection limits down to 2 ppm, at the expenses of weaker mechanical properties, which reduce the maximum pressure to 2 GPa.

New applications in Planetary and Earth sciences [60], Archaeometry [61,62], microelectronics [63], and biomedical sciences [64] confirm the new impact of this technique in various communities.

A natural evolution of XRF elemental mapping is the extension towards in-depth third dimension. The knowledge of the elemental variation along this third dimension intrinsically improves the data quality and therefore its interpretation. Compared to the standard absorption X-ray Computed Tomography, X-ray fluorescence computed tomography (XFCT) is more challenging since it is limited by self-absorption and matrix effect. Two strategies have been devel-

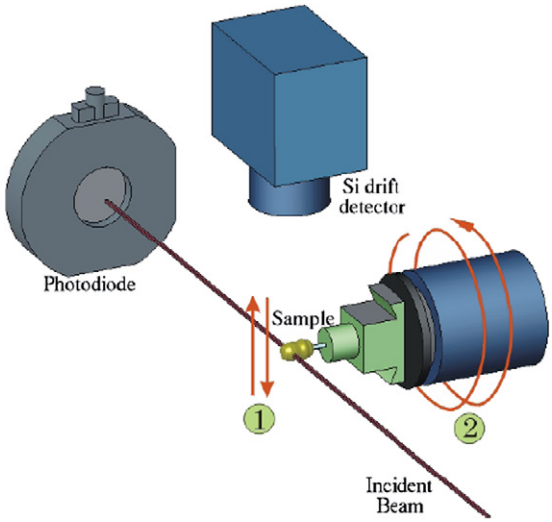

Fig. 10. An X-ray Fluorescence Computed Tomography (XFCT) setup: 1 and 2 show the sample movements to record a full 3D image by using a microbeam. The sample 'local' absorption, fluorescence and Compton scattering are recorded to produce this 3D chemical image.

oped to overcome these physical limitations. The first approach is based on an algorithm solution that relies on the combination of several signals (transmission, fluorescence and Compton) to derive the volumetric distribution of elements [65]. The second strategy, so-called confocal, is based on the use of two lens optics [66]. One lens (refractive lens) is used to focus the incoming beam and the second (polycapillary) restricts the detector angular acceptance to a small volume. The intersection volume of the incoming microbeam and the coinciding focus of the capillary lens determine the voxel size.

XFCT has the key advantage of providing three-dimensional (3D) quantitative images of a sample of a few hundreds of microns in size in a non-destructive way, while none of the other techniques are today capable of this suitable combination. The key application of XFCT is chemical imaging of high Z elements inside low Z matrices, i.e. imaging biological objects. However the technique can also find applications in nuclear imaging, environmental science, or geology. It has, for instance, been used to produce chemical images of fly ash particles created during the combustion process in power plants, and containing potentially toxic trace metals (like Pb, Cd, etc.) [67].

The XFCT geometry is essentially similar to the geometry of a 1st generation medical scanner. An energy sensitive detector records the fluorescence photons coming from the intersection line between the incoming X-ray pencil beam and the sample (see Fig. 10). By shifting the sample in the beam, a fluorescence projection line is progressively built, and a further sample rotation gives access to a full dataset of each chemical element after an appropriate data fitting. To move to 3D XFCT, one can repeat the same operation after selecting a new plane, or more elegantly use a helical path. As a matter of fact, the main problem in reconstruction from XFCT projections mainly comes from the absorption within the sample. Several reconstruction schemes have been proposed to solve this issue; one of the most successful one is the reconstruction algorithm developed by Golosio and coworkers [65], called ITT (Integrated Tomographic Techniques). It is based on a mathematical combination of three kinds of tomography, namely transmission, Compton and fluorescence tomography. The first one, transmission tomography, corresponds to standard absorption tomography that gives the distribution of the total absorption coefficient inside the sample. The second one, Compton tomography, is identical to fluorescence tomography as far as the geometry is concerned, except that the Compton signal is used. With appropriate reconstruction algorithms, Compton tomography can be used for reconstructing the distribution of the electronic density inside the sample. By combining mathematically transmission, Compton and fluorescence tomography, a quantitative 3D image (in g/cm^3) of the distribution of each chemical image can be reconstructed.

XFCT has two practical issues. The first one is the self-absorption. Although the ITT algorithm can correct for it, it will not give an exact quantitative image if the sample absorption is too high (e.g. sample with high Z matrices). Beside this, the scanning time can be prohibitive for some applications. For a 2D single slice acquisition, the scanning time is proportional to the size of the sample and inversely proportional to the X-ray spot size. To reach a 5 μm resolution, with a sample of 500 μm in diameter, 100 points will have to be recorded for each angle of view. It means that for

1 s exposure time (plus additional time due to data transfer and sample motion), 4 hours of synchrotron beamtime is necessary. To overcome this problem, multi-element detectors as well as fast and optimized scanning schemes are used, which can today enable fully 3D reconstructions of a sample within 24 hours.

4. Structure, crystallographic orientation and/or perfection

Bragg diffraction based synchrotron radiation imaging has proved to be able to provide information not available otherwise. This is due to the use of: (i) the coherence of the beam, as shown through the example of ferroelectric domains in poled crystals; and (ii) the parallelism of the beam coupled with new two-dimensional CCD detectors, which allow producing local rocking curves when using a monochromatic beam ('rocking curve imaging'). This 'local' behaviour gives clues to characterize the defects and/or understand the physical processes that occur in the crystal. Let us consider examples of these approaches.

4.1. Coherent beam Bragg diffraction imaging

When using a *coherent incident beam*, a series of features appear as phase objects for the diffracted beam: differences in thickness, pores, but also crystalline defects like defects stacking faults or antiphase boundaries. Poled ferroelectric domains in a single crystal, with periods in the 10 μm range, also constitute a phase grating for waves Bragg diffracted by the crystal. If the lateral coherence length is bigger than the period of the domains, the phase shift between the two types of domains can be directly obtained from the analysis of images recorded at various distances from the sample. The main contribution to this phase shift is associated with the variation of the phases of the structure factors, the two types of domains giving rise to a Friedel pair, exhibiting very similar modulus but different phases of the structure factors. This not only allowed to observe, on the surface [68] and the bulk [69] ferroelectric domains, like those observed on Fig. 11, but also to access to data at the atomic level, like the way these ferroelectric domains match on the domain wall.

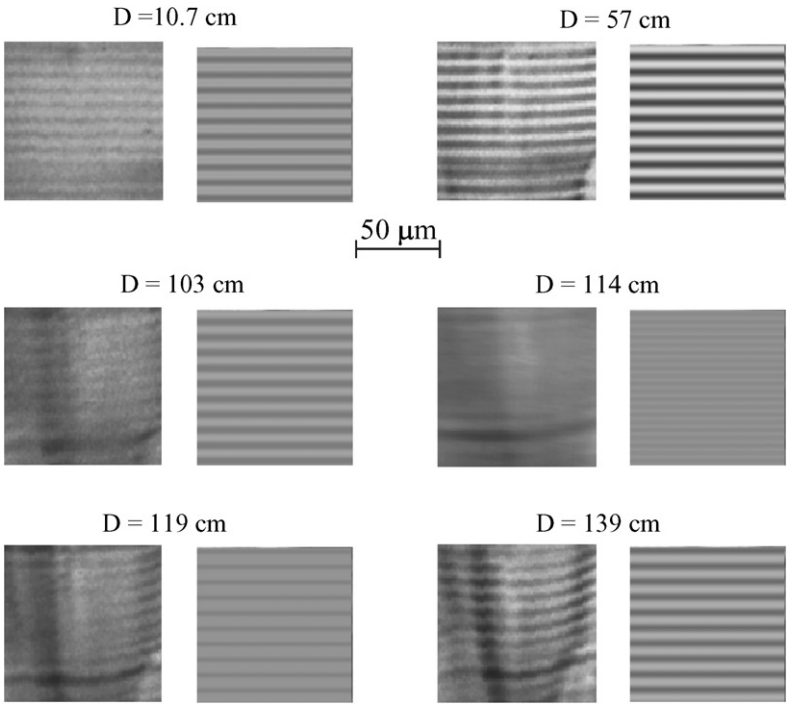

Fig. 11. 00ℓ reflection Bragg diffraction imaging with a coherent beam from a 9 μm periodically poled KTP crystal, for various sample-to-detector distances. Left: experimental images and Right: simulated image corresponding to periodic ferroelectric domains with (100) walls, in the case of the best fit among the various matching arrangements between domains. In addition deformation of the image and crystalline defects (vertical lines) are observed on the large distances experimental images, as well as, in the bottom area, a departure from the periodic arrangement of the domains.

Indeed several origins for additional phase shifts can be identified, but the only one that cannot be neglected is introduced by the way the domains match at the wall level. This very elusive information cannot be extracted, because it only entails a phase shift, from all previous diffraction and imaging experiments, not performed with a coherent beam. By comparing the experimental phase shifts with the phase jumps calculated for various models of the domain wall, the best fitting domain-matching model can be determined.

In the case of KTP (Potassium Titanium Oxide Phosphate ($KTiOPO_4$)) [70] the comparison of the experimental and the simulated intensity variations, at different distances, allows one to distinguish between the five possible domain-matching schemes, in which inversion domains are matched through Ti or P atoms of the unit cell. The phase shifts $\Delta\varphi$ between adjacent domain were calculated for each model from the complex structure factors of the 004 Friedel pair. The size and sign of $\Delta\varphi$ depend heavily on the position of the origin for this calculation, i.e. which atom was placed at the position $z = 0$, or, in other words, the way the domains match at the wall. The best fit of the observed modifications of the contrast as a function of distance was obtained for a $\Delta\varphi$ corresponding to one of the P atoms being the pivoting one for the twinning (simulations in Fig. 11). The simulation was performed using a perfect step function for the phase shift, the transition from $\Delta\varphi = 0$ to $\Delta\varphi \neq 0$ being abrupt, i.e. the displacement of unit cell atoms occurring at once from one cell to the next inverted one. The resulting model of twinning resulting is such that a perfect continuity of the major structural chains of PO_4–TiO_6 polyhedra along [100] is maintained across domain walls. It is worth noting that this information, at the atomic level, is obtained from images where the spatial resolution is in the μm range.

4.2. Rocking Curve Imaging

Bragg diffraction imaging applies, like all the other imaging techniques, to inhomogeneous samples. In most of the cases it is possible to associate a given region of interest (ROI) at the two-dimensional detector level with a region of the crystal, and therefore identify the regions of the crystal that produce contrast associated to a physical feature (defects, phase coexistence, domain boundary, etc.).

The 'Rocking Curve Imaging' [71], or 'Area Diffractometry' [72] technique was developed over the last few years on this principle to investigate quantitatively the distortions within a single crystal. A wide, monochromatic and parallel beam illuminates the sample, which is set to Bragg diffract for a given set of crystallographic planes. The diffracted beam is recorded on the CCD camera equipped with a scintillator and optics such that the effective pixel size is in the 1–10 μm range. The sample is rotated (angle ω) along the rocking curve, and images are recorded on various points of this rocking curve. This allows recording the 'local' rocking curve for a given (x, y) point of the crystal/detector. From this set of rocking curves many relevant data can be extracted: position of the peak, width of the peak, maximum or integrated diffracted intensity.

This is exemplified by the RCI study of a GaN crystal grown by epitaxial lateral overgrowth (ELO). GaN is an important material for applications in blue light emitting devices. The ELO process allows one to reduce the dislocation density of the GaN layers, and consequently improving the device efficiency. In the ELO process, the seed layer of GaN is covered by a thin amorphous mask layer exhibiting 'windows', as shown on Fig. 12. The subsequent growth of GaN proceeds preferentially from the windows areas, first vertically but also laterally, leading to T-shaped structures that ultimately coalesce and form a planar layer. The 'wings' of the T-shaped structure are of improved quality because the threading dislocations originating from the seed, which are detrimental for the device performances, are not able

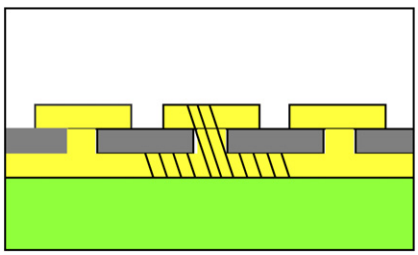

Fig. 12. Cross-sectional view of the ELO structure. A GaN layer (yellow on the figure) is deposited on a substrate (green on the figure), and is covered by a SiO_2 layer with windows (lateral periodicity 40 μm, grey on the figure). This structure reduces the number of dislocations, schematised by inclined lines, able to propagate during a further growth (also lateral) of the GaN layer above the windows.

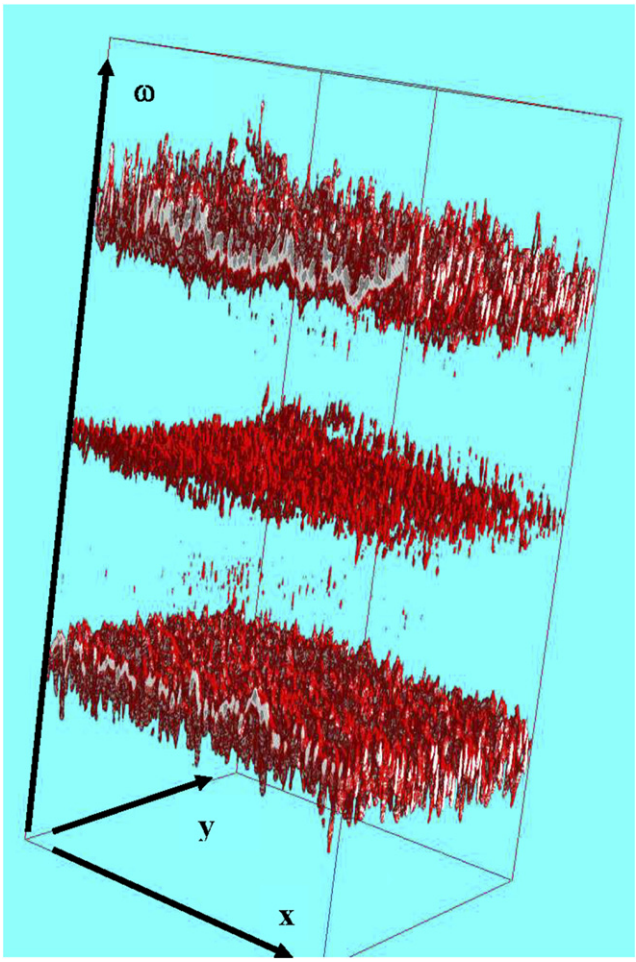

Fig. 13. 3D rendering of the local angle of the peak of the rocking curve for the substrate and the wings of a ELO produced GaN crystal (see text).

to propagate into these wings. It has been observed that these wings display a crystallographic tilt (some tenths of a degree) with respect to the initial GaN layer that can lead to defects when the various wings coalesce. Understanding this tilt can help avoid it, and improve the device characteristics. Fig. 13 shows a three-dimensional map (x, y, ω) of the diffracted intensity maximum position, which not only points out the lattice tilt (different ω) of the wings with respect to the substrate, but also the inhomogeneous distribution of local tilts, the actual 'local' quality, and the trend to an increased tilt when increasing the distance from the 'window' [73,74]. This type of work shows the potential of μm-resolved rocking curve imaging to disentangle complex phenomena.

A ROI within an image producing contrast can also be followed under the application of an external parameter (temperature, field, ...). The evolution of this ROI (image and/or local diffracted intensity) can give clues to understand the physical processes that occur in the crystal. An example of this approach is constituted by the identification of a broad interface between magnetic phases in MnP: the behaviour of this broad interface suggests that it is composed by a series of intermediate magnetic arrangements, that only exist during the phase coexistence, and which go from the ferromagnetic to the fan magnetic phases [75].

4.3. 3D characterization of the grain microstructure in polycrystals

The non-destructive characterization of polycrystalline materials in terms of grain shapes and crystallographic orientations constitutes a major experimental challenge in materials science. Currently two different approaches exist: (i) three-dimensional X-ray diffraction microscopy (3DXRD), a set of techniques which may be regarded as extensions

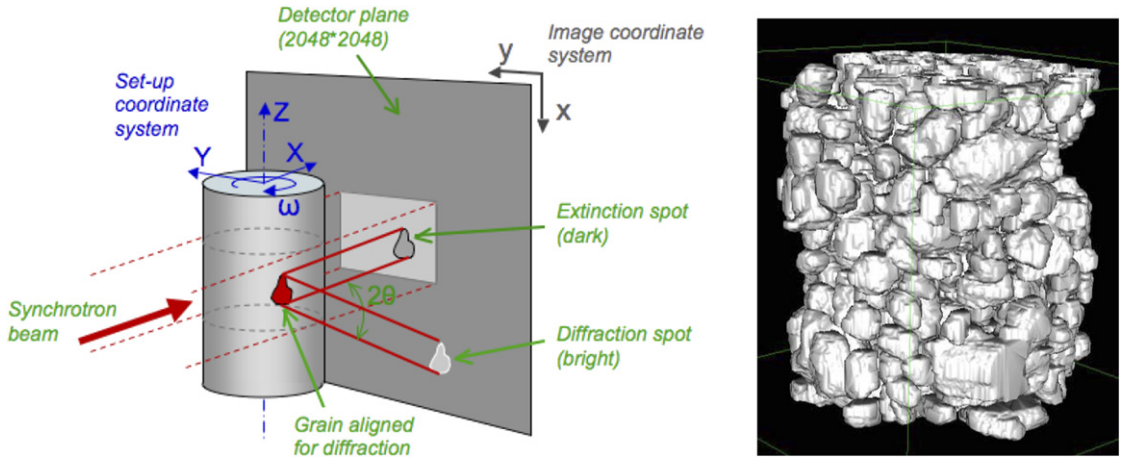

Fig. 14. (a) Overview of the acquisition geometry for diffraction contrast tomography. The footprint of the direct beam (light gray) fills only part of the field of the 2D detector system, which is set close to the sample in order to capture diffraction and absorption information, simultaneously; (b) 3D rendition of the reconstructed grain microstructure of a stainless steel wire sample, containing about 500 grains.

to the monochromatic beam rotation method (see e.g. [76] for a recent review); and (ii) differential aperture X-ray microscopy (DAXM) [77], a wire scanning method based on white beam Laue diffraction employing a point focused synchrotron beam.

Whereas 3DXRD allows for in-situ characterization of millimetre sized sample volumes (shape, orientation, average strain state of the grains) with a spatial resolution of the order of 5–10 μm, DAXM provides access to the local strain and orientation distribution of reduced sample volumes (typically tens of micrometers) with down to 1 μm resolution. However, neither of these diffraction techniques can provide information concerning the local composition of the material and/or the presence of defects inside the material. These complementary aspects of a material's microstructure can typically be imaged with the help of X-ray absorption or phase contrast microtomography (see e.g. [5] for a recent overview).

Here we present first results from a novel tomographic imaging technique, which combines the principles of X-ray absorption and X-ray diffraction imaging. The technique is termed diffraction contrast tomography (DCT) [78,79], underlining its similarity to conventional absorption contrast tomography with which it shares a common experimental setup. Applicable to the case of plastically undeformed, polycrystalline materials, the grains are imaged using the occasionally occurring diffraction contribution to the X-ray attenuation coefficient each time a grain fulfils the diffraction condition (Fig. 14). A large number of diffraction spots (up to several ten-thousands) are acquired on the 2D high resolution detector system situated closely behind the sample. With the help of an automated image analysis procedure [79] these diffraction spots are paired with their corresponding extinction contrast in the direct beam. Based on spatial as well as crystallographic constraints, the spot pairs are then sorted into sets, belonging to the same grain. Finally, the 3D shapes of each of these grains are reconstructed individually from the limited number of projections available (several tens per grain) using an algebraic reconstruction technique [80]. After re-assembling the grains into a common volume data-set, one may now visualise the 3D grain microstructure together with other features (e.g. cracks, inclusions), visible in the absorption image acquired at the same time. As an illustration, Fig. 14(b) shows a 3D rendition of such an reassembled grain volume taken from a 400 μm diameter stainless steel wire.

The technique is applicable to polycrystalline mono and multiphase materials and allows characterizing sample volumes containing several hundred grains in terms of 3D grain shapes (about 10 μm accuracy), crystallographic grain orientation (within 0.1 degree) and the 3D microstructure visible in X-ray absorption and/or phase contrast (defects, density variations, etc.). However, the current methodology requires the use of materials containing grains with low internal orientation spread (<0.5 degrees). In the case of metals, such low levels of orientation spread can typically only be found in recrystallization or solidification microstructures.

As possible applications one may, for instance, consider the characterization of undeformed, polycrystalline samples before exposing the material to chemical and/or mechanical degradation processes such as stress corrosion cracking or fatigue crack propagation (work in progress). The grain mapping, as well as the characterization of the

subsequent crack propagation can be performed on the same instrument, taking advantage of the in-situ imaging capability of state of the art microtomographic imaging instruments. Experimental data of this type are currently scarce and will provide invaluable input for various types of models and numerical simulations.

5. Conclusion

Micro-analytical and micro-imaging techniques aim at screening samples at various levels of information, ranging from elemental, chemical to structural and inhomogeneities. Most natural or man-made systems possess properties that almost always depend on the specific hierarchy of chemical components, and their organization at different length-scales. Therefore, an understanding of macroscopic function requires insights on microscopic structure and dynamics on all length-scales down to the molecular and atomic levels. The SR-based imaging and analysis techniques developed over the last years allow identifying the sample areas associated to a physical feature (density, orientation, composition, defects, etc.). They provide maps of the relevant parameters, or, increasingly, the local evolution of these parameters under the application of an external field (stress, temperature, electric or magnetic field, ..., or time). These investigations address a wide variety of topics, which include in-situ studies such as phase transformations, dynamics, reactions, simulated manufacturing conditions, deformation/damage, environment and cultural heritage related topics. The increasing use of these techniques by new scientific communities shows the need of pushing their temporal and spatial resolutions limits, but also indicates the trend for an increased automation.

References

[1] F. Adams, L. Van Vaeck, R. Barrett, Advanced analytical techniques: platform for nano materials science, Spectrochim. Acta B 60 (2005) 13.
[2] M.A. Marcus, A.A. MacDowell, R. Celestre, A. Manceau, T. Miller, H.A. Padmore, R.E. Sublett, Beamline 10.3.2 at ALS: a hard X-ray microprobe for environmental and materials sciences, J. Synchrotron Rad. 11 (2004) 239.
[3] J. Susini, M. Salomé, R. Tucoulou, G. Martinez-Criado, S. Bohic, D. Eichert, P. Bleuet, I. Letard, M. Cotte, J. Cauzid, B. Fayard, R. Baker, S. Labouré, X-ray micro-analysis activities at the ESRF, in: Proc. 8th Int. Conf. X-Ray Microscopy IPAP Conf. Series, vol. 7, 2006, p. 18.
[4] F. Peyrin, A.M. Charvet, La tomographie synchrotron, Traité IC2 "La tomographie", Editions Hermès, 2002, Chapter 15, p. 219.
[5] J. Baruchel, J.-Y. Buffière, P. Cloetens, M. Di Michiel, E. Ferrie, W. Ludwig, E. Maire, L. Salvo, Advances in synchrotron radiation microtomography, Scripta Mater. 55 (2006) 41.
[6] P. Tafforeau, R. Boistel, E. Boller, A. Bravin, M. Brunet, Y. Chaimanee, P. Cloetens, M. Feist, J. Hoszowska, J.-J. Jaeger, R.F. Kay, V. Lazzari, L. Marivaux, A. Nel, C. Nemoz, X. Thibault, P. Vignaud, S. Zabler, Applications of X-ray synchrotron microtomography for non-destructive 3D studies of paleontological specimens, Appl. Phys. A, Mat. Sci. Process. 83 (2006) 195.
[7] A. Pyzalla, D. Camin, T. Buslaps, M. Di Michiel, H. Kaminski, A. Kottar, A. Pernack, W. Reimers, Simultaneous tomography and diffraction analysis of creep damage, Science 308 (2005) 92.
[8] K. Uesugi, T. Sera, N. Yagi, Fast tomography using quasi-monochromatic undulator radiation, J. Synchrotron Rad. 13 (2006) 403.
[9] C. Scheuerlein, M. Di Michiel, A. Haibel, On the formation of voids in internal tin Nb3Sn superconductors, Appl. Phys. Lett. 90 (2007) 132510.
[10] S. Agliozzo, E. Brunello, H. Klein, L. Mancini, J. Härtwig, J. Baruchel, J. Gastaldi, Extended investigation of porosity in quasicrystals by synchrotron X-ray phase contrast radiography—I: in icosahedral Al–Pd–Mn grains, J. Cryst. Growth 281 (2005) 623.
[11] S. Agliozzo, J. Gastaldi, H. Klein, J. Härtwig, J. Baruchel, E. Brunello, In-situ study of the annealing behaviour of porosity in icosahedral Al–Pd–Mn quasicrystal using third generation X-ray synchrotron radiation imaging, Phys. Rev. B 69 (2004) 144204.
[12] J. Gastaldi, T. Schenk, G. Reinhart, H. Klein, J. Härtwig, N. Mangelinck-Noël, B. Grushko, H. Nguyen Thi, P. Pino, J. Baruchel, In situ observation of pore evolution during melting and solidification of Al–Pd–Mn quasicrystals by synchrotron X-ray radiography, Phil. Mag. 86 (2006) 335.
[13] Y.J. Wang, K.-S. Im, K. Fezzaa, W.K. Lee, J. Wang, P. Micheli, C. Laub, Quantitative X-ray phase contrast imaging of air-assisted water sprays with high Weber numbers, Appl. Phys. Lett. 89 (2006) 151913.
[14] P. Fenter, C. Park, Z. Zhang, S. Wang, Observation of subnanometre-high surface topography with X-ray reflection phase-contrast microscopy, Nature Phys. 2 (2006) 700.
[15] P. Cloetens, W. Ludwig, J. Baruchel, J.P. Guigay, P. Rejmankova-Pernot, M. Salomé-Pateyron, M. Schlenker, J.Y. Buffière, E. Maire, G. Peix, Hard X-ray phase imaging using simple propagation of a coherent synchrotron radiation beam, J. Phys. D: Appl. Phys. 32 (1999) A145.
[16] P. Cloetens, W. Ludwig, J. Baruchel, D. Van Dyck, J. Van Landuyt, J.P. Guigay, M. Schlenker, Holotomography: quantitative phase tomography with micrometer resolution using hard synchrotron radiation X-rays, Appl. Phys. Lett. 75 (1999) 2912.
[17] P. Cloetens, R. Mache, M. Schlenker, L. Lerbs-Mache, Quantitative phase tomography of Arabidopsis seeds reveals intercellular void network, Proc. Natl. Acad. Sci. 103 (2006) 14626.
[18] S. Zabler, P. Cloetens, J.-P. Guigay, J. Baruchel, M. Schlenker, Optimization of phase contrast imaging using hard X-rays, Rev. Sci. Instrum. 76 (2005) 1.
[19] J.P. Guigay, M. Langer, P. Cloetens, R. Boistel, Mixed transfer function and transport of intensity approach for phase retrieval in the Fresnel region, Opt. Lett. 32 (2007) 1617.

[20] R. Mokso, P. Cloetens, E. Maire, W. Ludwig, J.Y. Buffière, Nanoscale zoom tomography with hard X rays using Kirkpatrick–Baez optics, Appl. Phys. Lett. 90 (2007) 144104.
[21] D. Shapiro, P. Thibault, T. Beetz, V. Elser, M. Howells, C. Jacobsen, J. Kirz, E. Lima, H. Miao, A.M. Neiman, D. Sayre, Biological imaging by soft X-ray diffraction microscopy, Proc. Natl. Acad. Sci. 102 (2005) 15343.
[22] J. Miao, C.-C. Chen, C. Song, Y. Nishino, Y. Kohmura, T. Ishikawa, D. Ramunno-Johnson, T.-K. Lee, S.H. Risbud, Three-dimensional GaN–Ga2O3 core shell structure revealed by X-ray diffraction microscopy, Phys. Rev. Lett. 97 (2006) 215503.
[23] M.A. Pfeifer, G.J. Williams, I.A. Vartanyants, R. Harder, I.K. Robinson, Three-dimensional mapping of a deformation field inside a nanocrystal, Nature 442 (2006) 63.
[24] S. Eisebitt, J. Lüning, W.F. Schlotter, M. Lörgen, O. Hellwig, W. Eberhardt, J. Stöhr, Lensless imaging of magnetic nanostructures by X-ray spectro-holography, Nature 432 (2004) 885.
[25] H. He, U. Weierstall, J.C.H. Spence, M. Howells, H.A. Padmore, S. Marchesini, H.N. Chapman, Use of extended and prepared reference objects in experimental Fourier transform X-ray holography, Appl. Phys. Lett. 85 (2004) 2454.
[26] R.W. Gerchberg, W.O. Saxton, A practical algorithm for determination of phase from image and diffraction plane pictures, Optik 35 (1972) 237.
[27] J.R. Fienup, Phase retrieval algorithms: a comparison, Appl. Opt. 21 (1982) 2758.
[28] J.M. Rodenburg, A.C. Hurst, A.G. Cullis, B.R. Dobson, F. Pfeiffer, O. Bunk, C. David, K. Jefimovs, I. Johnson, Hard-X-ray lensless imaging of extended objects, Phys. Rev. Lett. 98 (2007) 034801.
[29] E. Lima, F. Glassmeier, F. Zontone, A. Madsen, unpublished.
[30] J. Miao, K.O. Hodgson, T. Ishikawa, C.A. Larabell, M.A. Legros, Y. Nishino, Imaging whole *Escherichia coli* bacteria by using single-particle X-ray diffraction, Proc. Natl. Acad. Sci. 100 (2003) 110.
[31] K.A. Taylor, R.M. Glasser, Electron diffraction of frozen, hydrated protein crystals, Science 186 (1974) 1036.
[32] M. Adrian, J. Dubochet, J. Lepault, A.W. McDowall, Cryo-electron microscopy of viruses, Nature 308 (1984) 32.
[33] T.J. Davis, D. Gao, T.E. Gureyev, A.W. Stevenson, S.W. Wilkins, Phase-contrast imaging of weakly absorbing materials using hard X-rays, Nature 373 (1995) 595.
[34] A. Bravin, Exploiting the X-ray refraction contrast with an analyser: the state of the art, J. Phys. D: Appl. Phys. 36 (2003) A24.
[35] D. Chapman, W. Thomlinson, R. Johnston, D. Washburn, E. Pisano, N. Gmür, Z. Zhong, R. Menk, F. Arfelli, D. Sayers, Diffraction enhanced X-ray imaging, Phys. Med. Biol. 42 (1997) 2015.
[36] E. Pagot, P. Cloetens, S. Fiedler, A. Bravin, P. Coan, J. Baruchel, J. Härtwig, W. Thomlinson, A method to extract quantitative information from analyser-based X-ray phase contrast imaging, Appl. Phys. Lett. 82 (2003) 3421.
[37] F. Arfelli, V. Bonvicini, A. Bravin, G. Cantatore, E. Castelli, L.D. Palma, M. DiMichiel, M. Fabrizioli, R. Longo, R.H. Menk, A. Olivo, S. Pani, D. Pontoni, P. Poropat, M. Prest, A. Rashevsky, M. Ratti, L. Rigon, G. Tromba, A. Vacchi, E. Vallazza, F. Zanconati, Mammography with synchrotron radiation: phase-detection techniques, Radiology 215 (2000) 286.
[38] E.D. Pisano, R.E. Johnston, D. Chapman, J. Geradts, M.V. Iacocca, C.A. Livasy, D.B. Washburn, D.E. Sayers, Z. Zhong, M.Z. Kiss, W.C. Thomlinson, Human breast cancer specimens: diffraction enhanced imaging with histologic correlation improved conspicuity of lesion detail compared with digital radiography, Radiology 214 (2000) 895.
[39] J. Keyriläinen, M. Fernández, S. Fiedler, A. Bravin, M.-L. Karjalainen-Lindsberg, P. Virkkunen, E.-M. Elo, M. Tenhunen, P. Suortti, W. Thomlinson, Visualisation of calcifications and thin collagen strands in human breast tumour specimens by the diffraction-enhanced imaging technique: a comparison with conventional mammography and histology, Europ. J. Radiol. 53 (2005) 226.
[40] E. Pagot, S. Fiedler, P. Cloetens, A. Bravin, P. Coan, K. Fezzaa, J. Baruchel, J. Härtwig, Quantitative comparison between two-phase contrast techniques: Diffraction Enhanced Imaging and Phase Propagation Imaging, Phys. Med. Biol. 50 (2005) 709.
[41] A. Bravin, J. Keyriläinen, M. Fernandez, S. Fiedler, C. Nemoz, M.-L. Karjalainen-Lindsberg, M. Tenhunen, P. Virkkunen, M. Leidenius, K. von Smitten, P. Sipila, P. Suortti, High-resolution CT by diffraction enhanced X-ray imaging: mapping of breast tissue samples and comparison with their histo-pathology, Phys. Med. Biol. 52 (2007) 2197.
[42] J. Mollenhauer, M.E. Aurich, Z. Zhong, C. Muehleman, A.A. Cole, M. Hasnah, O. Oltulu, K.E. Kuettner, A. Margulis, L.D. Chapman, Diffraction-enhanced X-ray imaging of articular cartilage, Osteoarthritis Cart. 10 (2002) 163.
[43] A. Wagner, M. Aurich, N. Sieber, M. Stoessel, W.-D. Wetzel, K. Schmuck, M. Lohmann, J. Metge, B. Reime, P. Coan, A. Bravin, F. Arfelli, G. Heitner, R. Menk, T. Irving, Z. Zhong, C. Muehleman, J.A. Mollenhauer, Options and limitations of joint cartilage imaging: DEI in comparison to MRI and sonography, Nuclear Instrum. Methods A 548 (2005) 47.
[44] P. Modregger, D. Lübbert, P. Schäfer, R. Köhler, Magnified X-ray phase imaging using asymmetric Bragg reflection: Experiment and theory, Phys. Rev. B 74 (2006) 054107.
[45] J.P. Guigay, E. Pagot, P. Cloetens, Fourier optics approach to X-ray analyser-based imaging, Opt. Commun. 270 (2007) 180.
[46] P. Coan, A. Bravin, Analysis of the X-ray refraction using an array-structured detector, Appl. Phys. Lett. 90 (2007) 184106.
[47] A. Olivo, F. Arfelli, D. Dreossi, R. Longo, R.H. Menk, S. Pani, P. Poropat, L. Rigon, F. Zanconati, E. Castelli, Preliminary study on extremely small angle X-ray scatter imaging with synchrotron radiation, Phys. Med. Biol. 47 (2002) 469.
[48] W. Chao, B.D. Harteneck, J.A. Liddle, E.H. Anderson, D.T. Attwood, Soft X-ray microscopy at a spatial resolution better than 15 nm, Nature 435 (2005) 1210.
[49] C. Schroer, B. Lengeler, Focusing hard X-rays to nanometer dimensions by adiabatically focusing lenses, Phys. Rev. Lett. 94 (2005) 054802.
[50] H. Hidekazu Mimura, H. Yumoto, S. Matsuyama, Y. Sano, K. Yamamura, Y. Mori, M. Yabashi, Y. Nishino, K. Tamasaku, T. Ishikawa, K. Yamauchi, Efficient focusing of hard X rays to 25 nm by a total reflection mirror, Appl. Phys. Lett. 90 (2007) 051903.
[51] H. Kang, J. Maser, G. Stephenson, C. Liu, R. Conley, A. Macrander, S. Vogt, Nanometer linear focusing of hard X rays by a multilayer Laue lens, Phys. Rev. Lett. 96 (2006) 127401.
[52] O. Hignette, P. Cloetens, G. Rostaing, P. Bernard, C. Morawe, Efficient sub 100 nm focusing of hard X rays, Rev. Sci. Instrum. 76 (2005) 063709.

[53] P.M. Bertsch, D.B. Hunter, Applications of synchrotron-based X-ray microprobes, Chem. Rev. 101 (2001) 1809.
[54] G.E. Ice, X-Ray Microprobe for Fluorescence and Diffraction Analysis, in: Methods in Materials Research: A Current Protocols Publication, John Wiley, New York, 1998.
[55] M. De Angelis, M.C. Morel-Fourcade, J.M. Barnola, J. Susini, P. Duval, Brine micro-droplets and solid inclusions in accreted ice from Lake Vostok (East Antarctica), Geophys. Res. Lett. 32 (2005) L12501.
[56] G. Martínez-Criado, R. Steinmann, B. Alén, A. Labrador, D. Fuster, J.M. Ripalda, A. Homs, S. Labouré, J. Susini, New cryogenic environment for beamline ID22 at the European Synchrotron Radiation Facility, Rev. Sci. Instrum. 78 (2007) 025106.
[57] N. Métrich, J. Susini, E. Foy, F. Farges, D. Massare, L. Sylla, S. Lequien, M. Bonnin-Mosbah, Redox state of iron in peralkaline rhyolitic glass/melt: X-ray absorption micro spectroscopy experiments at high temperature, Chem. Geol. 231 (2006) 350.
[58] C. Schmidt, K. Rickers, R. Wirth, L. Nasdala, J.M. Hanchar, Low-temperature Zr mobility: An in situ synchrotron-radiation XRF study of the effect of radiation damage in zircon on the element release in $H_2O^+HCl^{\pm}$ SiO_2 fluids, Amer. Mineralogist 91 (2006) 1211.
[59] P.M. Oger, I. Daniel, A. Picard, Development of a low-pressure diamond anvil cell and analytical tools to monitor microbial activities in situ under controlled P and T, Biochimica et Biophysica Acta 1764 (2006) 434.
[60] D. Brownlee, et al., Comet 81P/Wild 2 under a microscope, Science 314 (2006) 1711.
[61] M. Sandström, F. Jalilehvand, E. Damian, Y. Fors, U. Gelius, M. Jones, M. Salomé, Sulfur accumulation in the timbers of King Henry VIII's warship Mary Rose: A pathway in the sulfur cycle of conservation concern, Proc. Natl. Acad. Sci. USA 102 (2005) 14165.
[62] M. Cotte, J. Susini, A. Moscato, C. Gratziu, A. Bertagnini, N. Metrich, Blackening of Pompeian Cinnabar paintings studied by X-ray micro-spectroscopic imaging, Analyt. Chem. 78 (2006) 7484.
[63] G. Martínez-Criado, B. Alén, A. Homs, A. Somogyi, C. Miskys, J. Susini, J. Pereira-Lachataignerais, J. Martinez-Pastor, Scanning X-ray excited optical luminescence microscopy in GaN, Appl. Phys. Lett. 89 (2006) 221913.
[64] L. Finney, S. Mandava, L. Ursos, W. Zhang, D. Rodi, S. Vogt, D. Legnini, J. Maser, F. Ikpatt, O.I. Olopade, D. Glesne, X-ray fluorescence microscopy reveals large-scale relocalization and extracellular translocation of cellular copper during angiogenesis, Natl. Acad. Sci. USA 104 (2007) 2247–2252.
[65] B. Golosio, A. Somogyi, A. Simionovici, P. Bleuet, J. Susini, L. Lemelle, Nondestructive three-dimensional elemental microanalysis by combined helical X-ray microtomographies, Appl. Phys. Lett. 84 (2004) 2199.
[66] L. Vincze, B. Vekemans, F.E. Brenker, G. Falkenberg, K. Rickers, A. Somogyi, M. Kersten, F. Adams, Three-dimensional trace element analysis by confocal X-ray microfluorescence imaging, Analyt. Chem. 76 (2004) 6786.
[67] M.C. Camerani, B. Golosio, A. Somogyi, A.S. Simionovici, B.M. Steenari, I. Panas, X-ray fluorescence tomography of individual municipal solid waste and biomass fly ash particles, Analyt. Chem. 76 (2004) 1586.
[68] Z.H. Hu, P.A. Thomas, A. Snigirev, I. Snigireva, A. Souvorov, P.G.R. Smith, G.W. Ross, S. Teat, Phase-mapping of periodically domain-inverted $LiNbO_3$ with coherent X-rays, Nature 393 (1998) 690.
[69] P. Rejmankova-Pernot, P. Cloetens, J. Baruchel, J.P. Guigay, P. Moretti, Phase retrieval by combined Bragg and Fresnel X-ray diffraction imaging, Phys. Rev. Lett. 81 (1998) 3435.
[70] P. Pernot-Rejmankova, P.A. Thomas, P. Cloetens, T. Lyford, J. Baruchel, Structural matching of ferroelectric domains and associated distortion in KTP crystals, J. Phys.: Condens. Matter 15 (2003) 1613.
[71] D. Lübbert, C. Ferrari, P. Mikulík, P. Pernot, L. Helfen, N. Verdi, E. Villeggi, D. Korytár, T. Baumbach, Distribution and Burgers vectors of dislocations in semiconductor wafers investigated by Rocking Curve Imaging, J. Appl. Cryst. 38 (2005) 91.
[72] P. Mikulík, D. Lübbert, D. Korytár, P. Pernot, T. Baumbach, Synchrotron area diffractometry as a tool for spatial high-resolution three dimensional lattice misorientation mapping, J. Phys. D: Appl. Phys. 36 (2003) A74.
[73] D. Lübbert, P. Mikulík, P. Pernot, L. Helfen, M.D. Craven, S. Keller, S. DenBaars, T. Baumbach, X-ray microdiffraction imaging investigations of wing tilt in epitaxially overgrown GaN, Phys. Stat. Sol. (a) 203 (2006) 1733.
[74] P. Mikulík, D. Lübbert, P. Pernot, L. Helfen, T. Baumbach, Crystalline misorientation analysis in Ga-based wafers and ELO samples by rocking curve imaging, Appl. Surf. Sci. 253 (2006) 188.
[75] J. Baruchel, C. Medrano, M. Schlenker, Synchrotron radiation topographic study of the thick ferromagnetic-fan interface in MnP, J. Phys. D: Appl. Phys. 38 (2005) A67.
[76] H.F. Poulsen, 3D X-Ray Diffraction Microscopy, Springer Tracts in Modern Physics, Springer, Berlin, 2004.
[77] G.E. Ice, B.C. Larson, W. Yang, J.D. Budai, J.Z. Tischler, J.W.L. Pang, R.I. Barabash, W. Liu, Polychromatic X-ray microdiffraction studies of mesoscale structure and dynamics, J. Synchr. Rad. 12 (2005) 155.
[78] W. Ludwig, S. Schmidt, E.M. Lauridsen, H.F. Poulsen, Diffraction contrast tomography: a novel technique for 3D grain mapping in polycrystals. Part I: direct beam case, J. Appl. Cryst., submitted for publication.
[79] G. Johnson, A. King, M. Gonzalves-Hoennicke, W. Ludwig, Diffraction contrast tomography: a novel technique for 3D grain mapping in polycrystals. Part II: the combined case, J. Appl. Cryst., submitted for publication.
[80] R. Gordon, R. Bender, G.T. Herman, Algebraic reconstruction techniques (ART) for three dimensional electron microscopy and X-ray photography, J. Theor. Biol. 29 (1970) 471.